Chapter 2
Empirical Modelling of the Thermosphere

This chapter will describe the history, context, application and limitations of empirical thermosphere models. Section 2.1 will give an introduction to the atmospheric structure and variability. The observations of solar and geomagnetic activity that serve as drivers of thermosphere variability are presented in Sect. 2.2. Section 2.3 will provide a historical overview of model developments. The inner workings of the models, and the way they have been created, are described in Sect. 2.4. Section 2.5 provides an introduction to the concept of density model calibration, of which an implementation is described at the end of the thesis, in Chap. 6. This chapter ends with an overview of tools that are applied in the evaluation of density models and data sets in Sect. 2.6.

2.1 Atmospheric Structure and Variability

The Earth's atmosphere is often portrayed as a fragile, finite and thin layer of gases surrounding our planet. Since the number of atmospheric particles decreases exponentially with altitude, there is no definite boundary between the atmosphere and outer space. Even though the density at satellite altitudes (200 km and up) is at least a billion times lower than at sea level, the velocities of orbiting objects are so high that there is still a drag force that can often be measured by analysing satellite dynamics. This aerodynamic force can currently be derived from operational space surveillance satellite tracking orbit data for altitudes up to around 500 km and by using more specialised methods or equipment up to about 1500 km. Tracking measurements on the very first artificial satellites [50, 57] resulted in the identification of several important variations in density, which will be described in this Section.

Figure 2.1 shows how the main atmospheric layers are defined according to changes in the slope of the temperature profile. The maximum temperature is asymptotically reached in the topmost layer, the thermosphere. The level of the temperature in this region is highly dependent on the Sun, as will be explained in more detail

E. Doornbos, *Thermospheric Density and Wind Determination from Satellite Dynamics*, Springer Theses, DOI: 10.1007/978-3-642-25129-0_2,

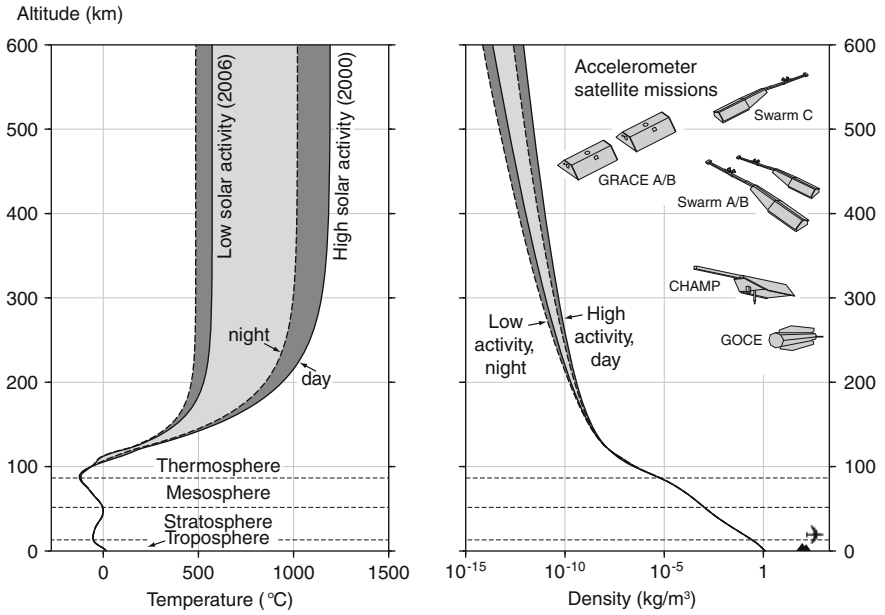

Fig. 2.1 Altitude profiles of atmospheric temperature (*left*) and density (*right*), according to the NRLMSISE-00 model, evaluated for 18:00 on July 15 2000 and 2006, over Delft, The Netherlands

below. The variations in temperature lead to variations in density, which can span several orders of magnitude.

2.1.1 Overview of Observed Density Variations

Figure 2.2 shows modelled density variations over an 11-year period, with two zoomed in views for 2000 and 2006. The NRLMSISE- 00 [76] model was evaluated at a single location: 400 km over Delft, The Netherlands. The major variations in density visible in this plot will be described below. A more detailed description of the drivers behind these variations will be provided in further sections of this chapter.

Diurnal and Seasonal Variations

First of all, uneven heating by the Sun of the spherical Earth causes the day-to-night variation in density, represented by the grey band in Fig. 2.2. This variation is also subject to seasonal changes, due to the movement of the sub-solar point as a result of the seasonally changing Sun-Earth geometry. In the thermosphere, the variation

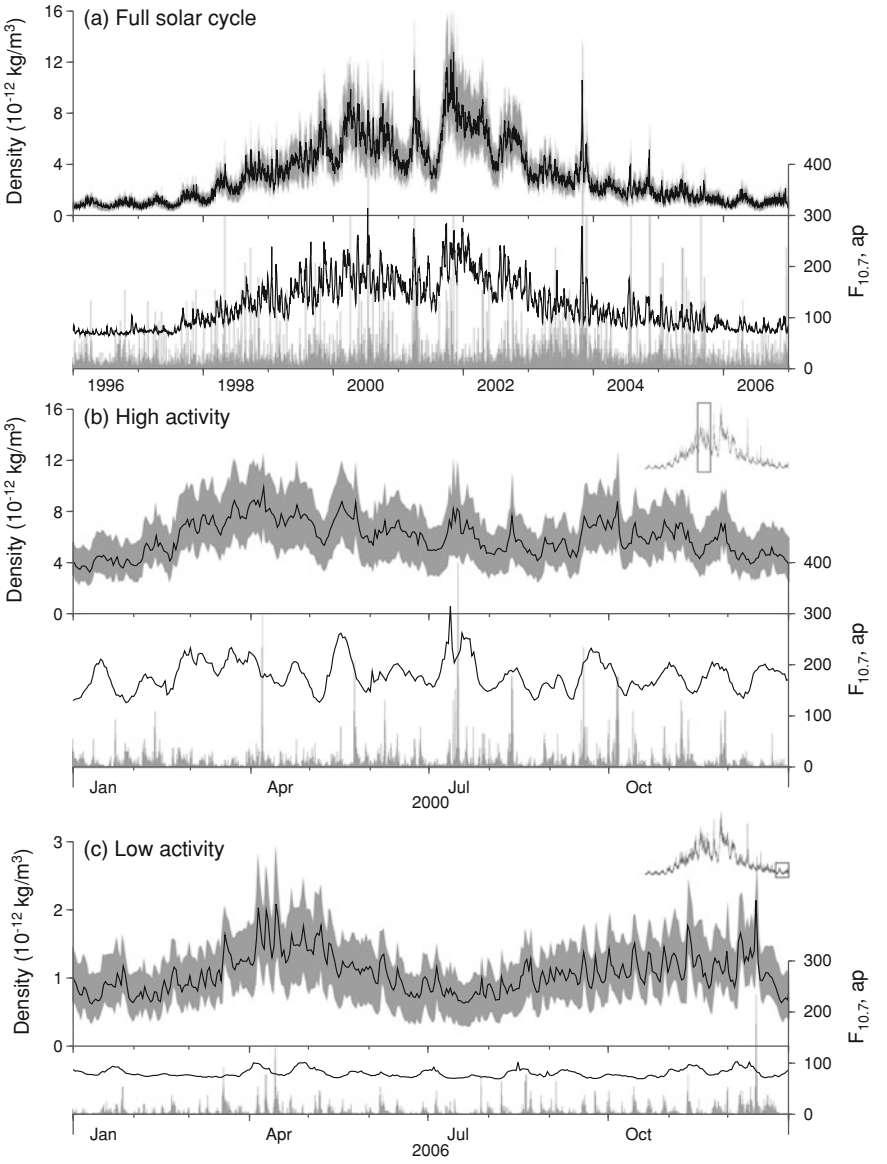

Fig. 2.2 Time series of modelled daily minimum and maximum (*grey area*) and average (*black line*) densities at 400 km over Delft. Time series of the solar and geomagnetic activity indices $F_{10.7}$ (*black line*) and ap (*grey spikes*), which drive the model, are plotted below each density time series

manifests itself in the form of a daytime density bulge, with a maximum following the sub-solar point with a time-lag of about two hours. In the horizontal plane, the density smoothly decreases to a minimum on the night side.

Because heating at the bottom of the thermosphere generally causes the entire thermosphere above this layer to expand, the day-night difference increases with altitude. It can be around a factor of 5 at 500 km and higher.

Solar Activity Variation

The second major variation in density is also related to the variation in heating of the thermosphere by solar radiation, but in this case it is not due to geometry but due to processes in the Sun. Although the level of solar radiation in the peak wavelengths of the visible spectrum is quite constant, the thermosphere absorbs only radiation at extreme ultraviolet (EUV) and X-ray wavelengths, which can be highly variable. The level of solar radiation at these wavelengths depends on the presence of active regions on the Earth-facing side of the Sun. Active regions are caused by local densifications in the magnetic field of the Sun. Sunspots often form in those areas.

During minima of the 11-year solar cycle period, there are fewer sunspots, and EUV output by the Sun is usually quite stable and at a low level. During solar cycle peak years however, the EUV output will be much higher and much more variable. This is due both to more rapid changes in the Sun's magnetic field, as well as due to the effect of solar rotation on the restricted view of the Sun's surface from Earth. After the 11-year cycle, the variability of received EUV radiation is most powerful at the period of the Sun's rotation, which is approximately 27 days.

The amplitude of the density variation due to variability in EUV radiation increases with altitude in the thermosphere. Between solar minimum and solar maximum, the density can vary by up to a factor of 20 at 500 km and higher.

The $F_{10.7}$ solar activity proxy (see Sect. 2.2.1) is used in current empirical models to drive this variation. This is apparent from the correlated behaviour of the black lines in Fig. 2.2.

Geomagnetic Activity Variation

Active regions are also related to the occurrence of solar flares and coronal mass ejections, which hurl great quantities of charged particles from the Sun into space. Near the Earth, these particles are mostly deflected by the Earth's magnetic field. Only a fraction can enter through the so-called polar cusps and via so-called reconnection processes at the dayside magnetopause, causing geomagnetic storms which are often accompanied by auroral displays. During these storms, a lot of additional energy is deposited in the polar thermosphere and ionosphere over a relatively short period of time. These sudden and short-lived events can cause density variations of up to one order of magnitude, dominating the normal diurnal variation. The relation of modelled density to peaks in the geomagnetic activity index *ap* (discussed in Sect. 2.2.2) is visible in Fig. 2.2. This relation will be shown in more detail in Sect. 2.2.3.

Semi-Annual Variation

The cause of the fourth major variation in thermospheric density has long been more elusive. The semi-annual variation, discovered by Paetzold and Zschorner [73], leads to density changes of about 30%, with maxima around April and October, although it can be quite irregular in both amplitude and phase [7]. During periods of low solar activity, it is the dominant cause of changes in density, as can be seen in Fig. 2.2. A possible physical explanation was proposed by Fuller-Rowell [34]. It involves an increased mixing of the major thermospheric species due to the uneven heating of the hemispheres at the solstices (the "thermospheric spoon"). This results in raised molecular oxygen and nitrogen and reduced atomic oxygen densities, which in turn lowers the density scale height and causes a compression of the atmosphere, independent of temperature variations.

2.1.2 Vertical Structure of the Atmosphere

By approximation, the pressure p, density ρ and temperature T of the Earth's atmosphere obey the ideal gas law,

$$\frac{p}{\rho} = \frac{RT}{M}, \tag{2.1}$$

where R is the universal gas constant ($8.314472\,\mathrm{J\,K^{-1}\ mol^{-1}}$) and M is the molecular weight of the gas. The vertical structure of the Earth's atmosphere is largely governed by *hydrostatic equilibrium*, a balance between the pressure pushing the gas out into space, and gravity, pulling it towards the Earth's surface. The hydrostatic equation relates the decrease of pressure p with height z to the density ρ and gravitational acceleration g:

$$\frac{dp}{dz} = -\rho(z)g(z) \tag{2.2}$$

Combining these two equations, atmospheric pressure can be expressed as a function of altitude:

$$p(z) = p(0)e^{-\int_0^z \frac{1}{H(r)}dr} \tag{2.3}$$

where H is the pressure scale height:

$$H(z) = \frac{RT(z)}{g(z)M(z)} \tag{2.4}$$

The variation of density with height can be derived similarly, resulting in:

$$\rho(z) = \rho(0)e^{-\int_0^z \frac{1}{H^*(r)}dr}, \tag{2.5}$$

with the density scale height H^* defined as

$$\frac{1}{H^*(z)} = \frac{1}{T(z)}\frac{dT(z)}{dz} + \frac{g(z)M(z)}{RT(z)} \tag{2.6}$$

For regions where temperature is constant, such as the upper thermosphere, the density scale height is equal to the pressure scale height. These scale heights, which depend on the temperature, represent the vertical distance over which the pressure or density decreases by a factor e. At sea level, the scale height is about 8.5 km, while in the thermosphere it is of the order of about 50 km.

Figure 2.1 shows the temperature and density profiles, according to the NRLMSISE- 00 model, for day and night conditions at very low and very high solar activity conditions. Below 100 km, a variety of heat sources and energy transport processes result in distinct temperature minima and maxima, which delineate the named layers of the atmosphere. With ascending altitude these are the *troposphere*, the *stratosphere* and the *mesosphere*. Our interest is in the top layer, the *thermosphere*, which is governed by the absorption of solar extreme-ultraviolet radiation, causing an asymptotically increasing temperature with altitude.

The Sun's radiation causes part of the gas particles in the thermosphere to become ionized, creating the Earth's *ionosphere*. Ionized particles and electrons tend to be greatly outnumbered by neutral particles, at least at altitudes below 800 km. Above that altitude, data on the composition of the thermosphere is very scarce. The presence of oxygen ions as a significant contributor to satellite drag is taken into account in the NRLMSISE- 00 model [76], but not in other models. In any case, the fact that charged particles are present in the upper atmosphere has a profound effect on the medium's electrical properties, which affect its heating and dynamics.

The *mean free path length* of the atmospheric gas is another important parameter. Below the thermosphere, the mean free path length is short, and there are many collisions between the gas molecules. This causes the constituents of the gas to remain well-mixed. This region is called the *turbosphere* or *homosphere*. In the *heterosphere*, collisions are much less frequent. The gases can separate through gaseous diffusion more rapidly than they are mixed by turbulence. According to Eq. 2.6, the density scale height of light-weight constituents is larger than for heavier constituents. Therefore, with increasing altitude, the major thermospheric species are molecular nitrogen (N_2), atomic oxygen (O), helium (He) and hydrogen (H), as can be seen in Fig. 2.3.

The *exosphere* is the region, above approximately 400–600 km (depending on the level of solar activity), from which particles may escape from the atmosphere. This occurs when the kinetic energy of the particle exceeds the gravitational binding energy, and if the mean free path length is long enough to prevent collisions with other particles.

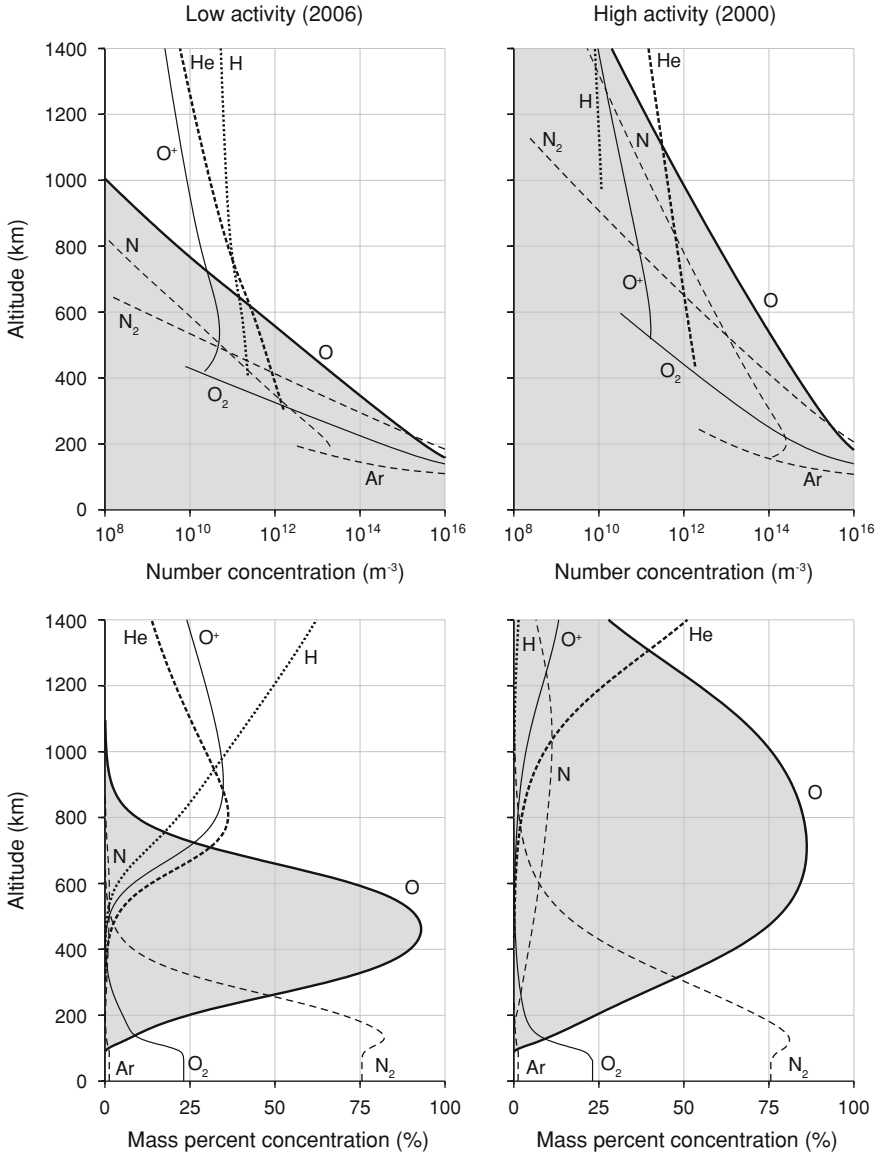

Fig. 2.3 Altitude profiles of atmospheric number concentrations (*top*) and mass percent concentrations (*bottom*), for low (*left*) and high (*right*) solar activity levels, according to the NRLMSISE- 00 model, evaluated over Delft, at 18:00 on July 15, 2000 and 2006

2.1.3 Energy Sources

The temperature profile of the atmosphere, discussed in the previous section, results from the balance between heat sources, loss processes and transport mechanisms. In the thermosphere, the most important sources of heat are solar EUV radiation, related to solar activity, and energetic charged particles, related to geomagnetic activity. Dissipation of tidal motions and gravity waves are minor heat sources, which are neglected in current empirical models. Heat is transported around and out of the thermosphere by conduction, radiation and convection.

For empirical modelling, the representation of density variations with solar and geomagnetic activity are of prime importance. They will be discussed in the next sections.

Solar EUV Radiation

The Sun emits electromagnetic radiation across a wide spectrum. At the wavelengths of visible light, where the solar irradiance is at its maximum, the emission is quite constant, but both at shorter wavelengths (ultraviolet) and longer wavelengths (radio), the level of emission is related to the level of activity of the Sun's magnetic field, and the interaction of this magnetic field with gases on the solar surface, the *photosphere*, and in its atmosphere, the *chromosphere* and *corona*. The emissions at the shortest wavelengths, of 170 nm and less, are responsible for heating the Earth's thermosphere. Radiation in this wavelength range is often designated extreme ultraviolet, or EUV radiation. Note that different publications might use slightly different definitions for the wavelength ranges in this part of the spectrum. The designations XUV (soft X-rays), EUV and FUV (Far Ultraviolet) may be encountered. In the following, we will avoid complications by simply using the term EUV for all solar radiation that heats the thermosphere.

The heating of the thermosphere by EUV radiation occurs through excitation, dissociation or ionization of the atoms or molecules (primarily O, O_2 and N_2). The excess energy of each photon is converted into kinetic energy of the reaction products. Rees [83] and Hargreaves [37] provide more detail about these processes.

Variations in EUV radiation are wavelength-dependent, as the shortest wavelengths are generally formed higher in the Sun's atmosphere and are more variable than longer wavelengths [59]. Radiation at different wavelengths is also generally absorbed at different altitudes in the Earth's atmosphere [78, 89]. Ideally, knowledge of the variability in irradiance over the entire UV and EUV spectrum is required in order to model the heating input in the atmosphere correctly.

The absorption of EUV radiation in the thermosphere results in a so-called diurnal bulge in temperature and density, on the daylight side of the Earth. For this reason, density variations in a horizontal plane are often mapped in a coordinate system of local solar time versus latitude (see Sect. 2.1.4). Local solar time (LST) is equivalent to the longitude coordinate on normal maps, but usually expressed in hours instead

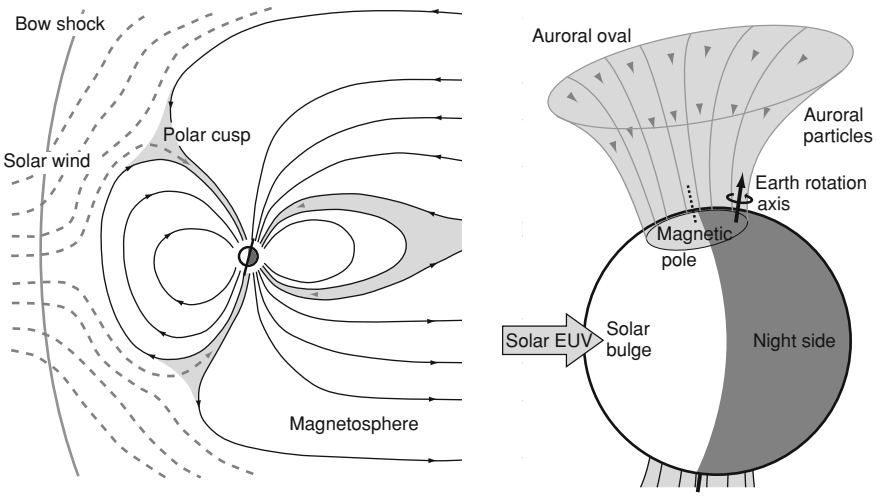

Fig. 2.4 Schematic views of the Earth's magnetosphere, the polar cusps and their relation with processes affecting thermosphere density variations

of degrees, and with the defining meridian, at 12 h (noon) LST, passing through the sub-solar point instead of through Greenwich. Due to thermal inertia, the diurnal bulge has its peak at around 14–15 h local solar time.

Solar Wind and Magnetospheric and Ionospheric Interactions

The Sun constantly emits a stream of particles out into space, called the *solar wind*. The solar wind consists mostly of electrons and protons, with a minor fraction of heavier ions [37]. The motion of these solar wind particles shapes the magnetic field of the Sun into the *interplanetary magnetic field*, which interacts with the terrestrial magnetic field, forming the Earth's *magnetosphere* (see Fig. 2.4). In effect, the terrestrial magnetic field shields the Earth from the solar wind. Solar wind particles can only enter the magnetosphere and upper atmosphere through the *polar cusps* and *reconnection processes* between the interplanetary magnetic field and the Earth's magnetic field.

During quiet times at the Sun, the solar wind originates mainly through *coronal holes*. These occur where magnetic field lines open up into interplanetary space. Sudden increases in the number of solar wind particles, and their speed, are related to *coronal mass ejections*, during which huge amounts of material are injected with high speed into the solar wind, and with *solar flares*, which are sudden short outbursts of electromagnetic energy and particles over a small area on the Sun. These phenomena are all closely related to the complexities of the Sun's magnetic field and occur more often during peak years of the 11-year solar activity cycle. The differences in speed between solar wind particles from various solar sources can cause interplanetary

shocks and compressions [37, 74]. The relationship between the Sun's magnetic field and these processes is the subject of ongoing investigations, with the aid of observatories on the ground and in space, including the SOHO [17] and STEREO [56] scientific satellite missions.

Near the Earth, the interactions between the solar wind, the magnetosphere and the ionosphere are complex. The solar wind particles are slowed down at the bow shock and are largely deflected around the magnetopause. They can only enter near the geomagnetic poles, i.e. approximately within the polar cap regions, where the Earth's magnetic field lines are open. Inside the magnetosphere, an extensive system of currents is present, as well as regions where charged particles are trapped. The system is complex, because the motion of the charged particles induces the currents and electric fields that in turn influence the magnetic field, which alters the motion of the charged particles. In the end, the processes on the Sun, which were briefly described above, can result in large disturbances at the Earth, called *geomagnetic storms* [e.g., 65, e.g., 35, e.g., 33, e.g., 94]. The physics of magnetospheric processes is a subject of intensive ongoing study. Moldwin [69], provides a basic introduction to the topic. Several space missions, including ESA's Cluster constellation [31], are helping to unravel the intricacies. These physical processes are studied by making use of extensive coupled thermosphere, ionosphere and magnetosphere models.

For the thermosphere, the most important aspect of this complex system is the mechanism in which energy is deposited. A relatively small part of this is due to particle precipitation. A larger contribution is due to Joule heating by ionospheric electric currents. The amount of energy deposited in the thermosphere through these two processes combined, normally amounts to about one fourth of the energy deposited by EUV radiation. After extraordinary large solar flares and coronal mass ejections, however, the energy deposited in the auroral zone can be up to twice that of the EUV energy [58].

Because there is an offset of the order of 10° between the dipole component of the Earth's magnetic field and its rotation axis (see Fig. 2.4), the location of maximum energy absorption in the auroral zone shows a diurnal shift when viewed in the local solar time versus geographic latitude reference frame. Variations in the thermosphere that are affected by geomagnetic activity are therefore often calculated and viewed in a system of geomagnetic coordinates.

2.1.4 Horizontal Structure

Now that the different energy inputs have been introduced, it is possible to have a look at how they affect variations in the thermosphere in a horizontal plane. Figures 2.5 and 2.6 show temperatures, densities and wind speeds from the NRLMSISE- 00 [76] and HWM- 93 [45] models, at 400 km altitude above the Earth's surface. Figure 2.5 shows the situation at low solar activity, when solar EUV radiation is the dominant energy source. Figure 2.6 shows the situation for the exact same time of day and day of year, only six years earlier. The factors influencing the diurnal and seasonal

variation are exactly the same, however the energy input is completely different. The $F_{10.7}$ proxy has a three times higher value in 2000, compared with 2006. Even more importantly, the snapshot of model values in Fig. 2.6 is taken at the peak of a major geomagnetic storm. How these circumstances affect the temperature, density and wind speeds will be explained in the following paragraphs.

Temperature and Density Variations at 400 km Altitude

The diurnal bulge, caused by EUV heating, is the dominant feature in the horizontal plane for temperature and density at low solar activity as seen in the top two frames of Fig. 2.5. The maximum density, at around 1.2 10^{-12} kg/m^3, is located several hours East of the sub-solar point. It is summer in the Northern hemisphere, and the maximum temperature there is around 900 K. The temperature minimum, of around 600 K is close to the South Pole.

At high solar and geomagnetic activity, Joule heating and particle precipitation in the auroral zones have become the dominant energy sources, so that the diurnal variation is hardly visible anymore. Temperatures have become twice as large as at solar minimum, and now there are maxima around both the Poles. The temperature minimum is located near the night-side equator.

The density at high solar activity is more than a factor 10 larger than at low activity. The density maximum has shifted towards the auroral zone, while there are now minima at mid-latitudes on the night-side.

These Figures are just snapshot images of the model at specific moments in time. Although the NRLMSISE- 00 model shows increased variability during this geomagnetic storm, compared to low activity conditions, its spatial resolution is actually quite coarse when compared with density observations derived from accelerometer measurements, as will be shown in Chap. 5.

Horizontal Winds in the Thermosphere

The bottom two rows in Figs. 2.5 and 2.6 show horizontal wind speeds and directions at 400 km altitude, obtained from the HWM- 93 model. This model outputs zonal and meridional wind speeds, with respect to a corotating atmosphere. The wind direction at the Poles is therefore undefined.

The third row in the Figures shows just the output of the model, which is a representation of the wind that could be measured by an observer on the ground. The bottom row adds the speed of the Earth's rotation to the output of the model. This is a representation of the wind that influences the motion of satellites. The corotation velocity is proportional to the cosine of the latitude, which goes from a maximum at the equator (483–502 m/s at altitudes of 250–500 km) to zero at the poles. Figure 2.5 shows that the HWM- 93 output is below 200 m/s and is therefore quite small compared to the corotation velocity at low latitudes. The deviation from corotation becomes more important in the polar areas, and at high activity, as can

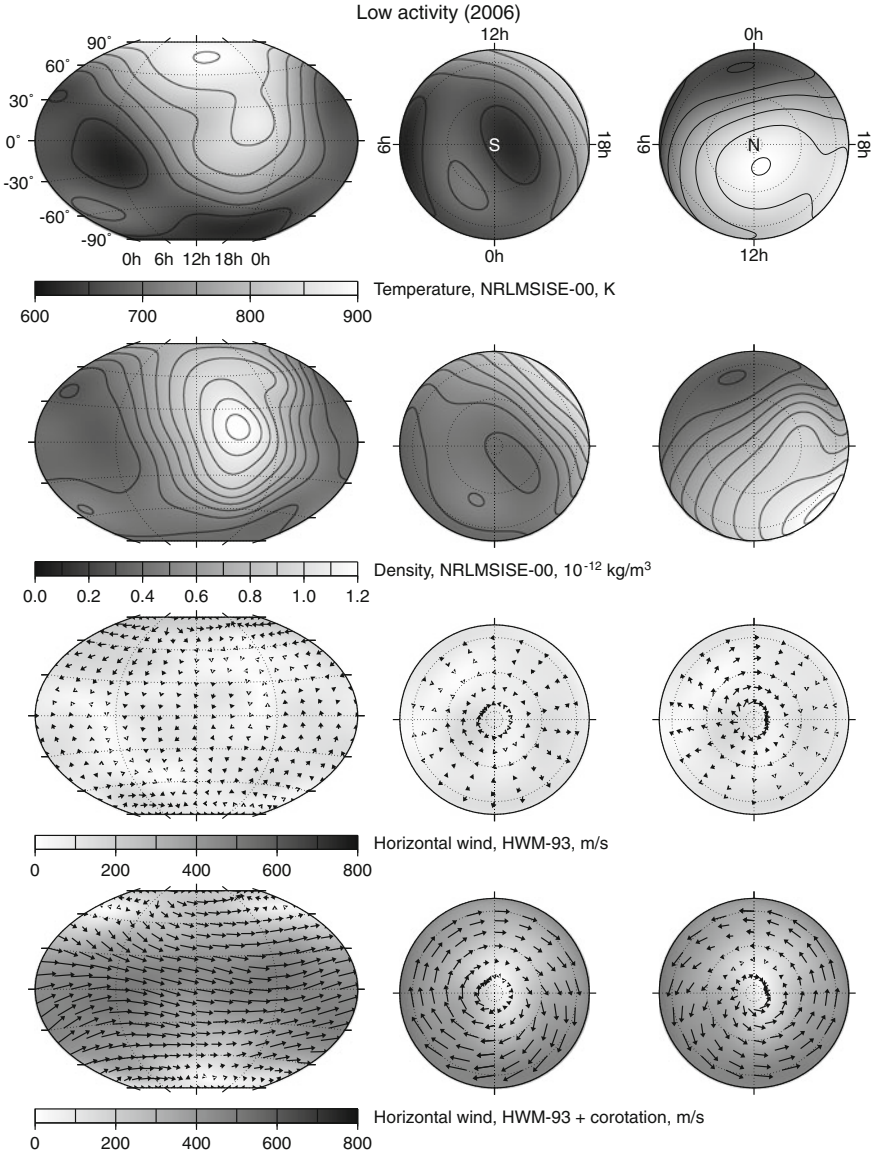

Fig. 2.5 Maps of modelled temperature, density and wind speeds at 400 km altitude, on July 15, 2006 at 18:00:00 UTC ($F_{10.7}$ = 70.2, ap = 3). The map projections are, from *left* to *right*, a Winkel Tripel projection, and two orthographic hemispherical projections centered on the geographic South Pole and North Pole

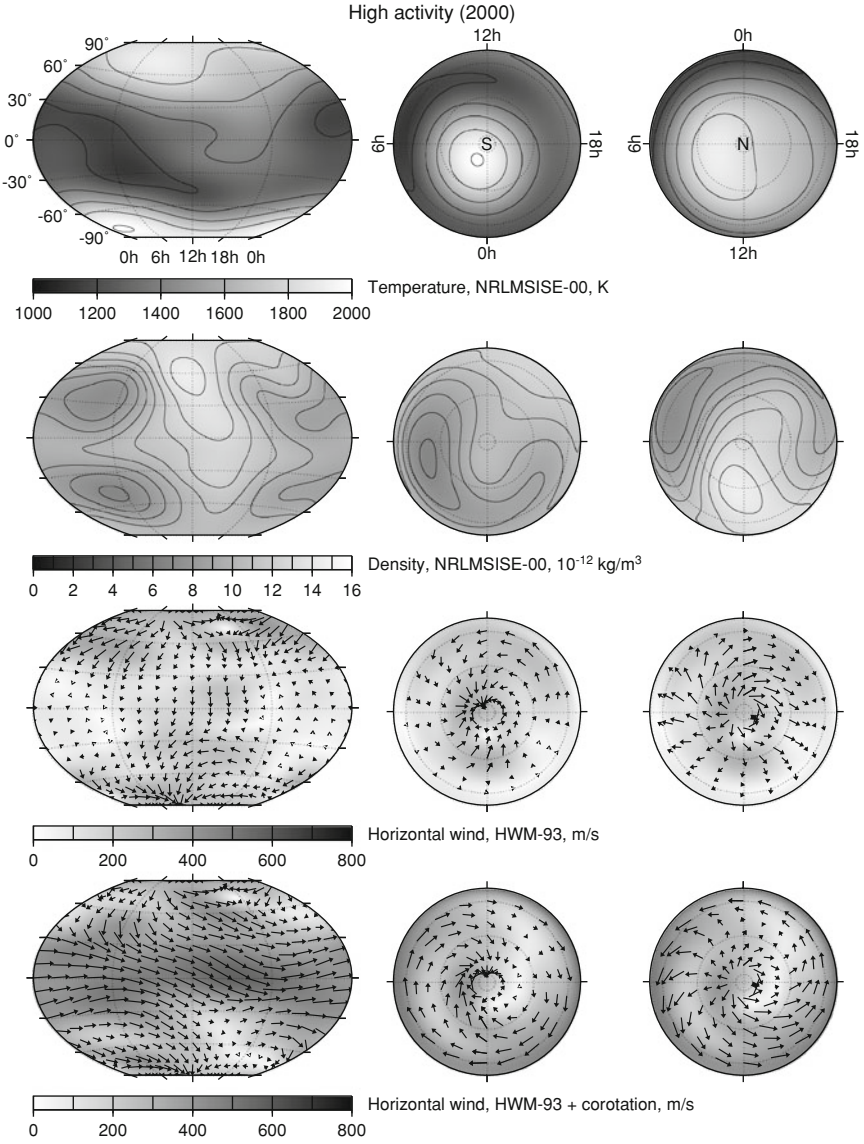

Fig. 2.6 Same as Fig. 2.5, but for July 15, 2000 at 18:00:00 UTC ($F_{10.7}$ = 213.1, ap = 400)

be seen in Fig. 2.6. Unfortunately, the observation data at high latitudes on which models such as HWM- 93 are based, is quite sparse. Accelerometer-derived wind data, if properly calibrated, could be very helpful in that respect.

Altitude Dependence of the Horizontal Density Structure

Figures 2.1 and 2.3 have provided a representation of the variation of density with height at a single location, while Figs. 2.5 and 2.6 have shown the variations in the horizontal plane at a single altitude level of 400 km. Now, in Fig. 2.7, both views are combined, to get a more coherent picture of density variations in the thermosphere.

It is clear from the Figure that the situation at 400 km is quite representative for a large range in altitude. This is especially true at low solar activity, when the diurnal bulge is the dominant feature. However, at 100 km, *semi-diurnal tides* dominate. In this region, the behaviour of the thermosphere is tightly linked to that of the mesosphere, and density levels are actually lower during solar maximum than at solar minimum, according to the model.

The behaviour of total density above approximately 600–800 km is also quite different. There is a distinct density peak over the winter hemisphere. This *winter helium bulge* is caused by the atmospheric dynamics of lower altitudes [64], where helium is a minor constituent. The minor light-weight gas is dragged along with the circulation of the major gas flow at lower altitudes, but because of its large scale height, more helium is transported to the winter pole than is returned to the summer pole [13].

2.1.5 Temporal Variability

Up to this point, the figures in this Section have focussed on two distinct times with extreme low and high solar and geomagnetic activity conditions. To complete our overview of the major variations in the thermosphere, we go back to Fig. 2.2, which showed the magnitude of the day-to-day variability of density over the course of the a solar cycle, and zoomed in views for the years 2000 and 2006, as modelled by NRLMSISE- 00. During the year 2000, the approximately 27-day solar rotation period is a dominant feature in both $F_{10.7}$ and density. During the more quiet year of 2006, the semi-annual variation with maxima in April and October is more clearly visible, and the relative effect of occasional peaks in geomagnetic activity are larger. Note for example the three peaks in April 2006.

2.2 Observations, Proxies and Indices of Thermospheric Energy Inputs

In the previous Section, the large influence of processes on the Sun, in the magnetosphere and in the ionosphere on the thermosphere has been explained. Therefore, observations of these processes are very useful in order to study and model the

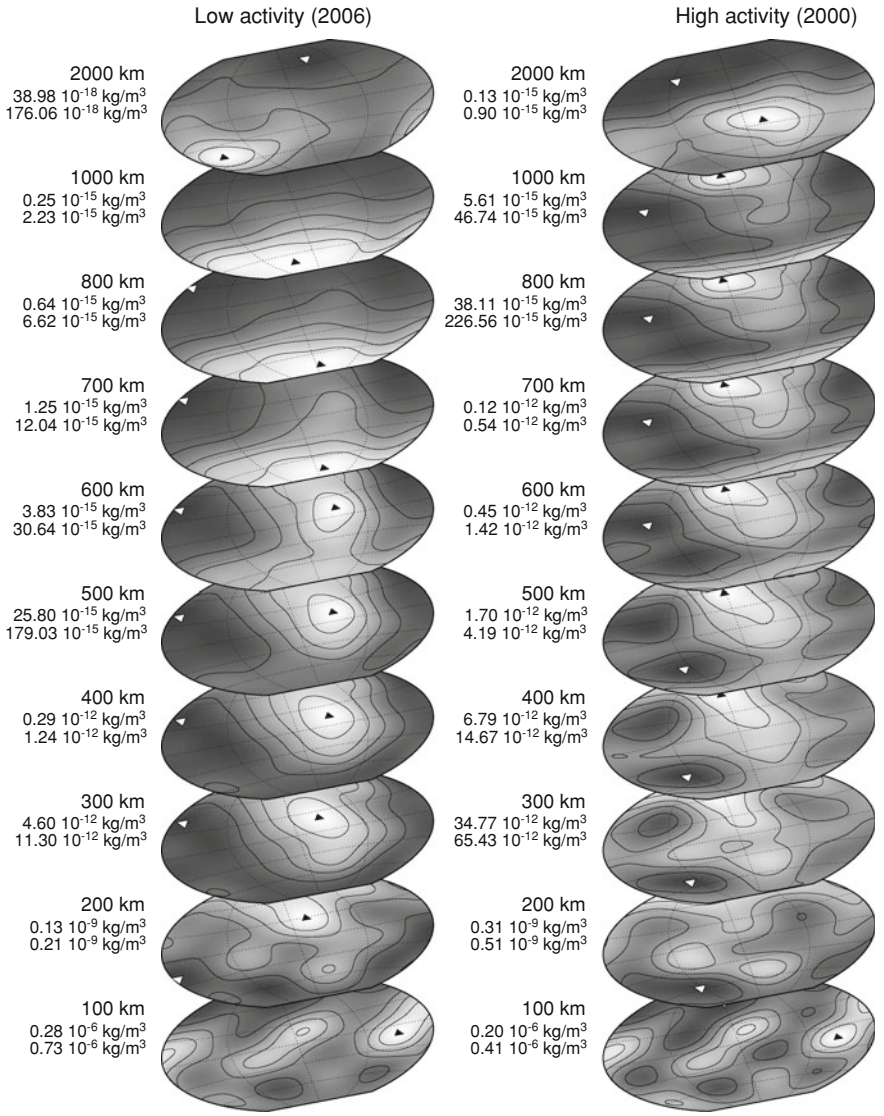

Fig. 2.7 Maps of modelled density on July 15, 2006 at 18:00:00 UTC (*left*) and at the same date and time in 2000 (*right*). The locations of the absolute minimum and maximum values at each altitude are indicated by the white and *black triangles*, respectively. The corresponding values are provided alongside the maps. Contour lines are drawn at 20% intervals between the minimum and maximum.

thermosphere. These observations are often available in the form of *proxies* and *indices*. A proxy is an observation that is related to, and shows similar behaviour as the phenomena of interest, but that is easier to obtain, or for which the historical

record is more complete, than a direct observation. An index is a quantity that is derived from observations according to a pre-designed standard. Indices are often designed to summarize complex phenomena from multiple observations, facilitating the representation in models and the quick identification of disruptive events.

2.2.1 Solar EUV Observations and Proxies

Measurements of the Sun's radiative output at EUV wavelengths are difficult, as they need to be made by satellites above the absorbing atmosphere. To make matters worse, instrumentation sensitive to this radiation also degrades significantly under its influence [32, 59]. Measurements from satellites started in the 1960s, but they have only been available on a regular basis since the 1990s. These recent missions have also introduced calibration techniques to account for the effects of instrument degradation. Such missions include UARS [82], launched in 1991, SOHO [17], launched in 1995, TIMED [75], launched in 2001 and SORCE [85], launched in 2003.

It is important to note that investigations on the thermosphere before the 1990s had to be made without reliable direct and continuous observations of variations in EUV radiation, contemporaneous with the available data on density. Instead, investigators had to rely on observations of solar activity in parts of the spectrum that are available on the ground, such as the number of sunspots visible on the solar disc, or the level of radiation at radio-wavelengths, which can be used as proxies for the EUV radiation.

10.7-cm Radio Flux

Sunspot numbers have been recorded since their first observation by Galileo in 1610, but a better correlation with thermospheric density was found with $F_{10.7}$ [50], which is the amount of energy received from the Sun at 10.7 cm wavelength. $F_{10.7}$ measurements have been made daily by radio telescope, operated by the National Research Council at Ottawa from 1947 to 1991 and at Penticton, British Columbia from 1991 onwards. $F_{10.7}$ is always supplied in units of 10^4Jansky (Jy) $= 10^{-22}$ W/m^2 /s. In plots and publications, the units are usually omitted, or designated simply as solar flux units (sfu). The proxy ranges from below 70 during solar minimum, to around 370 during extremely active days.

Early researchers such as Jacchia [50] first recognized the solar radiation influence on the thermosphere from the 27-day variations which were found in orbital drag time series. It was later found that a more slowly varying component of solar radiation was also present. The moving average of $F_{10.7}$ over three or four solar rotations (81 or 108 days), denoted $\bar{F}_{10.7}$ was used to represent this component.

The $F_{10.7}$ data are published in two forms: the *observed* fluxes are the actual measured values, while the *adjusted* fluxes are scaled to a standard distance of 1 AU, to compensate for the varying distance between the Earth and Sun through the year.

While the adjusted values give a better representation of the processes taking place on the Sun, the observed values better represent the EUV heating input in the upper atmosphere. Therefore, the latter should be used as input to the density models.

Mg II Core-to-Wing Ratio

It is now widely recognized that the use of $F_{10.7}$ and $\bar{F}_{10.7}$ as proxies in empirical density models has become a limiting factor in further improving their accuracy. With the availability of better satellite observations and empirical models of solar irradiances, researchers have started looking for alternative, more representative proxies, of which the most widely studied example is Mg II.

The use of the Mg II core-to-wing ratio (or just Mg II for short), was first proposed by Heath and Schlesinger [39], and is computed by taking the ratio of the intensity of the Mg II emission at 280 nm over that of the nearby line wings. The use of this ratio makes the index much less sensitive to instrument trends, since the wavelength dependence on degradation is limited. Mg II observations have been made from various satellites with different instrument characteristics. From these different datasets, composite time series have been constructed that often do not go further back than the 1990s. These time series correlate well with $F_{10.7}$. For density studies, the Mg II time series are often scaled using linear regression with $F_{10.7}$ so that they can be expressed in the same units.

Combinations of EUV Proxies

Of specific interest with regard to the use of EUV measurements for thermosphere modelling is the work by Dudok de Wit et al. [28], who performed a principal component analysis on EUV spectra recorded by the TIMED satellite. An important result of this analysis is that the full EUV spectrum can be reconstructed with high accuracy from just a small number of spectral lines. The work confirms that a single spectral line or proxy is clearly not sufficient to represent variability at the different wavelengths within the EUV spectrum that affect the thermosphere. This technique provides graphical representations of the similarity and dissimilarity of the behaviour of the various spectral lines and EUV proxies.

The use of a combination of proxies for representing EUV input in the thermosphere has been the strategy of Tobiska et al. [89] and Bowman and Tobiska [6] in preparation for the JB2006 density model. After testing several combinations, they arrived at the use of $F_{10.7}$, Mg II and S_{EUV}, and their 81-day averages. The S_{EUV} index is a measure of the integrated 26–34 nm emission, observed by SOHO. The Mg II and S_{EUV} measurements have been averaged to daily values and converted by linear regression to the same value range as $F_{10.7}$, resulting in the new indices $M_{10.7}$ and $S_{10.7}$. For the update of the Jacchia-Bowman model to its 2008 version, JB2008 [9], an additional solar activity index was added, designated $Y_{10.7}$. It is a composite index, designed to represent 0.1–0.8 nm X-ray emissions during solar maximum and

Lyman-α emissions during moderate and low solar activity. Separately from these modelling efforts, solar indices have recently been analysed by Guo et al. [36] using CHAMP accelerometer observations.

2.2.2 Geomagnetic Activity Observations and Indices

Satellite observations of charged particles from the solar wind and their interaction with the magnetosphere have been available since the late 1970s and early 1980s. These observations were made from NOAA's TIROS and POES satellites, as well as by the DMSP program [58]. More recently, observatories of the Sun, the magnetosphere and the interplanetary environment such as SOHO, ACE, Cluster and STEREO, have greatly increased our knowledge of these complex environments and their interactions.

These measurements have never been used in empirical thermosphere models though. Thermosphere models have traditionally made use of the *Kp* and *ap* geomagnetic indices, which are extensively described in the monograph by Mayaud [63], and the more accessible review article by Menvielle and Berthelier [66]. The information in this section draws heavily from these sources.

The *Kp* and *ap* Geomagnetic Indices

The *Kp* index is derived from measurements made at 11 geomagnetic observatories at mid-latitudes, through a rather intricate procedure, described by Menvielle and Berthelier [66]. At these stations, the horizontal magnetic components are separated in regular and irregular variations. The intensity of the irregular variations is expressed in a *K* index at each station, over each three-hour period.

This *Kp* index, as defined by Bartels et al. [3], ranges from 0 to 9, in discrete steps of one third, specified by plus and minus signs, as follows: 00, 0+, 1−, 10, 1+, …, to 90. The *K* indices from the 11 stations are standardized to avoid local time influences and averaged to form the planetary index *Kp*. Since *Kp* is a true index, it carries no physical units. It can be converted to the approximate amplitude of geomagnetic perturbation by the use of a conversion table, resulting in *ap* (planetary equivalent amplitude) values, expressed in units of nanoTesla (nT). These *ap* values should be multiplied by two to represent the magnitude of the observed variation in the magnetic field. Since the *ap* index is related directly to *Kp*, it also has a 3-hourly cadence, and can take no other values than those 27 listed in the *Kp* to *ap* conversion table. The average of all eight *ap* values in a UTC day is denoted as the *Ap* index. Time series of *Ap* can be useful for creating plots and quickly identifying active days, but the loss of temporal resolution with respect to *ap* makes the daily index less suitable for use in density models.

Alternative Geomagnetic Indices

Kp and related indices are widely used in many applications, including thermosphere models. However, by today's standards, they show some obvious shortcomings [66, 67]. Since the *Kp* network was set up at the start of the cold war period, most stations are located in Western Europe and North America. Relatively minor magnetic disturbances over one of these areas will therefore result in high values of the index, while disturbances of similar magnitude in uncovered areas might go largely unnoticed.

A new global network, with a much better geographical distribution, was set up after the International Geophysical Year (1957/1958), coinciding with the beginning of the space age. The *an*, *as* and *am* indices, all expressed in nT are derived from the *K* indices measured at these stations. The *an* index represents the northern hemisphere, *as* the southern, and *am* (where *m* stands for 'mondial') is the average of both hemispherical indices. The *am* index can therefore be considered an improved version of *ap*.

The *longitude sector geomagnetic indices*, or aλ indices, are *K*-derived indices which are provided for various pre-defined longitude sectors [68]. Five of these sectors, each of which contains two or more observing stations, are in the Northern hemisphere, and four are in the Southern. These indices are thus able to represent variations with longitude.

Other parameters, such as the *Dst* (*disturbance storm time*) and *PC* (*polar cap*) indices represent only certain parts of the geomagnetic activity, at low and high latitudes respectively, which are mainly driven by distinct current systems. See, for example, Campbell [14], Troshichev et al. [90], Asikainen et al. [1] and references therein. These two indices are available at an hourly or higher rate and therefore offer improved temporal resolution compared to the 3-hourly *K*-derived indices. Knipp et al. [58] provide an empirical model for the power input by Joule heating in the thermosphere, based on quadratic equations using these two indices.

2.2.3 Comparison of Proxies and Indices

Figure 2.8 shows a comparison of time series of several of the proxies and indices described in the previous Sections, along with densities derived from the accelerometer observations by CHAMP and GRACE. During the period of late October to the end of November 2003, the variations in solar activity were especially large, due to the presence of large active regions on the surface of the Sun (see Fig. 2.2 for context). Two of the largest geomagnetic storms of the solar cycle occurred during the last days of October, and on 20 and 21 November. Note that the behaviour of these indices during this time period is not necessarily indicative for other time periods.

The bottom panel in the plot shows the variation of the four daily solar radiation proxies that are provided for the JB2008 model. During this period, $F_{10.7}$, which is used by older models as well, shows the largest amplitude. The $M_{10.7}$ and $S_{10.7}$

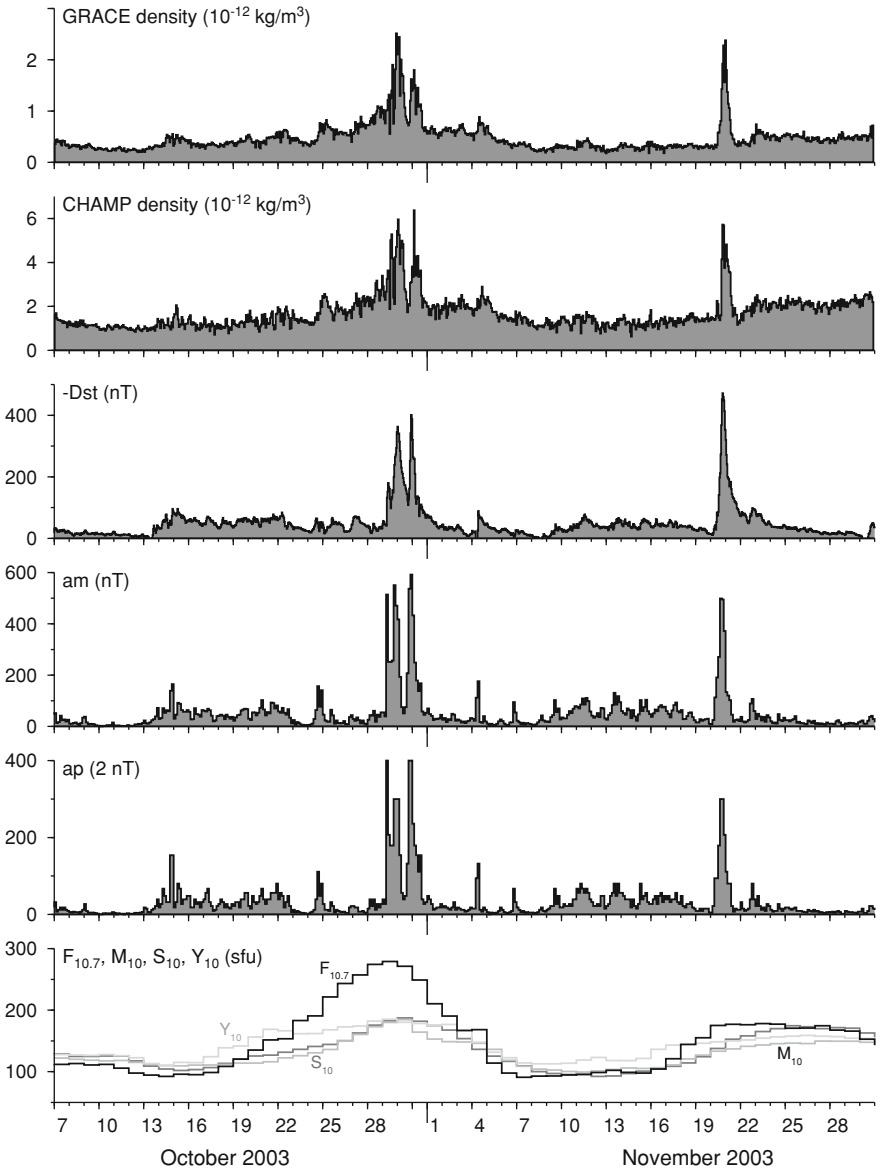

Fig. 2.8 Comparison of orbit-averaged densities from CHAMP and GRACE with geomagnetic indices and solar activity proxies

proxies, introduced with the JB2006 model, show similar values during low activity, but differences are considerable around the time of the storms. The $Y_{10.7}$ proxy, which was a new addition in the JB2008 model shows an earlier onset of the two periods of increased activity during these months.

Three other panels in Fig. 2.8 show the hourly *Dst* and the three-hourly *am* and *ap* indices. The *am* and *ap* profiles look quite similar. The main difference between these indices is in the improved global distribution of the observation network for the *am* index. The result of this is especially apparent in the relative magnitudes of the three peaks of the October storm. The *Dst* index, which returns predominantly negative values, has been multiplied by -1 here for easier comparison with the other indices. *Dst* provides more detail, because of its hourly rate, but it only represents the geomagnetic disturbances in the equatorial region. After major disturbances, *Dst* takes longer to recover than the *am* and *ap* values. Notice also how the disturbance on October 24 is not clearly present in the *Dst* plot, and how the maximum amplitude of the November storm exceeds that of the October storm in *Dst*, but not in *am* or *ap*.

From this example and the discussion in the previous Sections, it is clear that there is a wide variety of observations, proxies and indices available for research in thermospheric density and its connection to processes on the Sun. In the early 1960s, the combination of $F_{10.7}$ and *ap* was chosen to represent all non-periodic variations in density. This was a convenient choice, because long time series for these values were already easily available at the time. Empirical modellers have stuck to this choice until the recent introduction of new proxies and indices with the JB2006 and JB2008 models.

2.3 Empirical Density Models

The development of new density models has been largely driven by the availability of new sources of observation data. With the availability of more data, the models have become able to represent more subtle variations in density. Table 2.1 lists the most widely known models and their references. Jacchia, MSIS and DTM are the three major families of models, which have been under development since the 1960 and 1970s. Several models of these families will be evaluated and used in this research, and they are therefore introduced in the remainder of this chapter.

2.3.1 Early Models and Jacchia's Models

The first observations of orbital motions of satellites under the influence of drag in the late 1950s paved the way for the first generation of general empirical density models in the 1960s and early 1970s. Examples of these models include those by Harris and Priester [38] and Jacchia [51–53, 55]. The Jacchia-71 model was adopted as the COSPAR International Reference Atmosphere in 1972, and is therefore also known as CIRA- 72 [54]. Later models by Jacchia, such as those published in Jacchia [55], have not led to accuracy improvements with respect to this model [61]. The Jacchia-70 and -71 models have been used as the basis of the NASA Marshall Engineering Thermosphere (MET) models [49, 72], which have been applied in satellite lifetime

Table 2.1 List of empirical thermosphere models, their literature references, and the source of the FORTRAN code for the models that have been obtained and implemented for use and evaluation in this study

Model family	*Model name*	*Reference*	*Source code*
Jacchia	Jacchia-64	Jacchia [51]	
	Jacchia-70	Jacchia [52]	
	Jacchia-71	Jacchia [53]	
	Jacchia-Roberts-71	Roberts [84]	
	CIRA-72	Jacchia [54]	In reference
	Jacchia-77	Jacchia [55]	
	MET	Hickey [49]	
	MET 2.0	Owens [72]	
	JB2006	Bowman et al. [10]	Internet[1]
	JB2008	Bowman et al. [9]	Internet[2]
DTM	DTM	Barlier et al. [2]	In reference
	DTM-94	Berger et al. [4]	From author
	DTM-2000	Bruinsma et al. [11]	
MSIS	MSIS	Hedin et al. [43, 44]	
	MSIS-83	Hedin [40]	
	MSIS-86	Hedin [46]	Internet[3]
	CIRA-86	Hedin [41]	
	MSISE-90	Hedin [42]	
	NRLMSISE-00	Picone et al. [76]	Internet[3]
HWM	HWM-87	Hedin et al. [47]	
	HWM-90	Hedin et al. [48]	
	HWM-93	Hedin et al. [45]	Internet[4]
	HWM07	Drob et al. [27]	Internet[4]
	DWM07	Emmert et al. [30]	Internet[4]
	Harris-Priester	Harris and Priester [38]	
	TD88	Sehnal [86]	
	GOST	see Vallado [91, App. B]	
	GAMDM	Emmert and Picone [29]	In reference

[1] http://sol.spacenvironment.net/$\sim$\ignorespacesjb2006/
[2] http://sol.spacenvironment.net/$\sim$\ignorespacesjb2008/
[3] http://uap-www.nrl.navy.mil/models_web/msis/msis_home.html
[4] http://uap-www.nrl.navy.mil/models_web/hwm/hwm_home.html

predictions. More recently, Jacchia's models have been further improved under an initiative of the US Air Force Space Command, with new algorithms for computing the semi-annual density variation and the use of additional solar and geomagnetic activity proxies. This effort has resulted in the Jacchia-Bowman 2006 (JB2006) and 2008 (JB2008) models [9, 10].

2.3.2 DTM Models

The first of the DTM models was published in 1978 [2]. Like the Jacchia models, DTM was based solely on observations of satellite drag and neutral atmospheric temperatures, however it used a more generalised model formulation. A major update, named DTM- 94, was published by Berger et al. [4]. DTM- 94 is based on an extended satellite drag dataset for improved accuracy at solar minimum and solar maximum conditions. It included Dynamics Explorer 2 mass spectrometer and CACTUS accelerometer data as well. DTM model improvement efforts continued with the introduction of the Mg II solar EUV proxy [88] in DTM- 2000 [11] and incorporation of new data such as those from the CHAMP accelerometer [12].

2.3.3 MSIS and HWM Models

Starting in the late 1970s Alan Hedin created a new class of density models, named MSIS. His models [43, 44] were based solely on mass spectrometer and incoherent scatter radar observations. The main advantage of the use of these datasets over the drag-derived datasets is that they consist of independent observations of both temperature and number densities for the atmospheric constituents. The MSIS- 86 model replaced Jacchia-71 as the COSPAR International Reference Atmosphere thermosphere model, and is therefore also known as CIRA- 86 [41, 46]. An extension to the model was published as MSISE- 90 [42]. This model is identical to MSIS- 86 for the thermosphere region, but extends down to zero altitude.

At the end of the 1990s, development of the MSIS-class models was continued at the US Naval Research Laboratory (NRL). The resulting NRLMSISE- 00 model [76] includes additional mass spectrometer and incoherent scatter radar data, as well as accelerometer data and the DTM and Jacchia satellite orbit decay databases. An additional constituent, anomalous oxygen, was introduced in the model to investigate apparent discrepancies between the datasets at higher altitudes.

The HWM series of thermospheric horizontal wind models was created alongside the MSIS model series. The model subroutine accepts the same inputs as the MSIS series of density models and returns zonal and meridional wind speeds. The models are based on gradient winds from CIRA- 86 plus rocket soundings, incoherent scatter radar, MF radar and meteor radar data. Further development of the HWM model series is now also continued at the Naval Research Lab. The latest edition is HWM07 [27], which has a companion model for high geomagnetic activity, the Disturbance Wind Model DWM07 [30].

2.4 Empirical Model Implementations and Limitations

The empirical models considered in this chapter were all created by fitting a set of parametric equations to an underlying database of observations. The accuracy of the models is therefore dependant on both the strength of the database as well as the ability of the parametric equations to reproduce these data for interpolation and extrapolation. There are considerable differences between the number and complexity of the parametric equations used in the various models. Full details on the model formulations and generation can be found in the references provided in Table 2.1. However, a few details which are of importance for this study will be provided here.

2.4.1 Jacchia's Algorithm

In short, the Jacchia models use the exospheric temperature T_∞ as a defining parameter. This temperature is calculated for each location from the solar activity data, in combination with a model of the diurnal variation. Additional corrections are applied, depending on time and altitude. These include the semi-annual variation, a seasonal-latitudinal variation and an additional geomagnetic activity term. The exospheric temperature is then used as input for a temperature profile, which forms the basis for the integration of the diffusion equation.

The first step in the CIRA- 72 density computation is the calculation of the culmination point temperature. This temperature, denoted by T_c, is the night-time minimum of the global exospheric temperature field, when the geomagnetic index K_p is zero. It is a function of the solar activity proxy and its 81-day average, and three empirical constants (α, β and γ):

$$T_c = \alpha + \beta \bar{F}_{10.7} + \gamma (F_{10.7} - \bar{F}_{10.7}) \tag{2.7}$$

T_c is then multiplied with the diurnal variation function $D(t, \phi, lst)$. This function, which does not depend on the solar or geomagnetic activity, defines the shape of the diurnal bulge for the model, as shown in Fig. 2.9. It provides a smooth variation between the minimum temperature T_c and a maximum temperature of 1.3 times T_c to the East of the sub-solar point.

The calculation of the local exospheric temperature T_∞ is completed by adding a temperature correction for geomagnetic activity, ΔT_G

$$T_\infty(t, \phi, \lambda) = T_c(t)\ D(t, \phi, \lambda) + \Delta T_G(a_p) \tag{2.8}$$

Jacchia's temperature profile is further defined by a boundary condition of $T = 183\,K$ and $dT/dh = 0$ at the minimum altitude of 90 km and an inflection point at an altitude of 125 km. The inflection point temperature T_x is a function of T_∞ and four empirical constants (a, b, c and k)

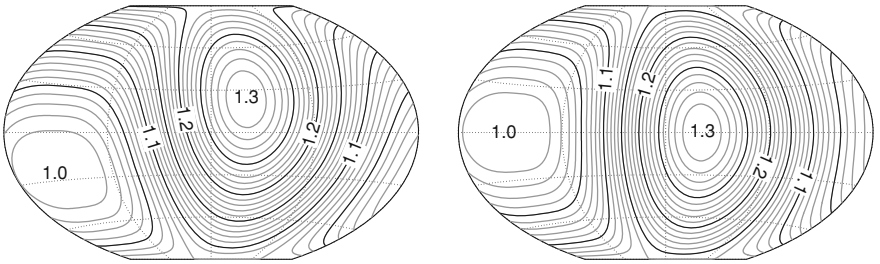

Fig. 2.9 The CIRA–72 diurnal temperature function at solstice (*left*) and equinox (*right*). The map is a Winkel-Tripel projection in local solar time versus latitude

$$T_x(T_\infty) = a + bT_\infty + c\ \exp(kT_\infty) \tag{2.9}$$

With the complete temperature profile now in place, the model computes the number density of each individual species by integrating the diffusion equation. The density output is completed by adding the empirical corrections for geomagnetic activity variation, the semi-annual variation and seasonal-latitudinal variation.

2.4.2 The DTM and MSIS Algorithms

In the DTM and MSIS models, the temperature profile with height is a function of the exospheric temperature. Just as in Jacchia's model, the exospheric temperature is determined from solar and geomagnetic activity proxies and indices. Unlike Jacchia's models, however, the density in the DTM and MSIS models is not derived from a direct integration with altitude over the temperature profile. Instead these models basically contain independent sub-models for the thermospheric temperature, T_∞, and number densities, n_i, of each of the constituents. The index i is used to iterate over each of the atmospheric constituents (H, He, O, etc.), and a set of model coefficients a_j (with $j = 0 \ldots N$) is defined for the temperature and densities of each of the constiuents. We will use the notation and equations from the DTM- 94 model [4] in this Section. The formulation for the thermospheric part of the MSIS models is largely similar. The modelled thermospheric temperature and concentrations are expressed using a function $G(L)$ of the input parameter vector L as follows

$$T_\infty = a^0_{T_\infty}(1 + G_{T_\infty}(L)) \tag{2.10}$$

$$n_i(z) = a^0_i \exp(G_i(L))\, f_i(z) \tag{2.11}$$

where $f_i(z)$ is the altitude law, based on the integration of the differential equation of diffusive equilibrium (see Berger et al. [4] for details).

The total density can then be computed from the concentrations by multiplying with the molecular mass m_i of the constituents and summing all constituents.

$$\rho_i = \frac{m_i n_i}{N_A} \tag{2.12}$$

$$\rho = \sum_i \rho_i \tag{2.13}$$

where $N_A = 6.022\ 10^{26}$ kmol^{-1} is Avogadro's number.

The functions $G(L)$ can contain a large number of terms, for instance:

- Polynomial terms with the solar and geomagnetic activity proxies and indices,
- Spherical harmonic terms in geomagnetic latitude and geomagnetic local time,
- Periodic terms in day of year and time of day, and
- Cross terms of solar and geomagnetic activity with the periodic variations.

The coefficients for these terms have been determined in a least squares adjustment using a large database of density and temperature measurements. There is a large difference between the complexity of the DTM models and that of the MSIS models. This is mainly due to the fact that the MSIS models incorporate many more variations of density and temperature in the lower atmosphere. As an example, the DTM- 94 model is defined by 172 non-zero coefficients, while the NRLMSISE- 00 model requires approximately 2,200.

2.5 Density Model Calibration

The density observations that will be derived using the algorithms presented in Chap. 4 have many applications in space physics research. Ultimately, such research should result in updated, more accurate empirical and physical models of the thermosphere. This generally requires the availability of other types of data, as well as expertise from other disciplines, such as solar irradiance monitoring and thermosphere-ionosphere-magnetosphere coupling. These are exciting fields of research, but due to their extent they must largely remain outside the scope of the remainder of this thesis.

There is, however, a simpler and less time consuming way in which the density observations derived from satellite dynamics can contribute to the improvement of empirical density models and their applications in operational and precise orbit determination. This is done by assimilating the density data in an adjustment of the empirical model output. This process, which will be introduced below, has become known as empirical density model calibration. The output of the HASDM calibrated model will be used to evaluate density measurements in Chap. 5, while an independent implementation of the calibration technique, developed under contract for the European Space Operations Centre ESOC, will be the main subject of Chap. 6.

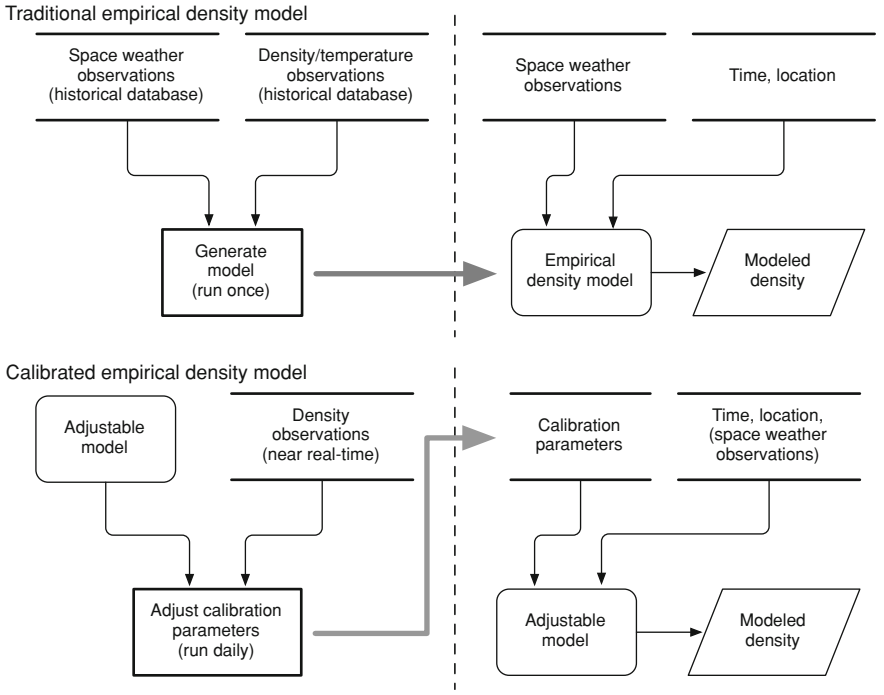

Fig. 2.10 Flow chart of traditional empirical density model creation and use (*top*), compared with that of a near real-time calibrated density model (*bottom*). The model generation or calibration procedure is displayed on the *left*, the use of the model in applications on the *right*

2.5.1 Approach

In order to calibrate an empirical density model, adjustable correction parameters that influence the model output have to be made available in the interface of the model's source code implementation. Optimal values for these correction parameters can be determined using a least-squares minimisation of density observation residuals. The estimated correction parameters can then correct or even replace the role of solar and geomagnetic activity indices in driving the irregular variations in the density model.

For use in operational applications, such as re-entry prediction and collision avoidance, the estimation of calibration parameters must be performed in near real-time, preferably at regular intervals, such as daily or 3-hourly. Figure 2.10 shows the flow chart of this process in the bottom panel, to be compared with the traditional one-time generation of a new version of an empirical model in the top panel.

Even though the original empirical model that is being adjusted still requires space weather proxies and indices as inputs, the calibration process should be able to absorb most of the shortcomings in the correlation between the proxies and indices and the density. The calibration parameters, estimated from satellite drag data, there-

fore largely replace the role of these space weather observations for the historical representation of the atmospheric state. Using this method, a significantly better level of accuracy than that of the uncalibrated empirical models can be reached.

The concept of empirical density model calibration was first published by Marcos et al. [62]. Shortly afterwards, two distinct density calibration initiatives were started by scientists in the space tracking community.

2.5.2 US-Russian Collaborative Density Calibration Project

A United States-Russian collaborative density calibration project involved the estimation of daily scale factors, varying linearly with altitude, which multiply the original model density to better represent orbit data. The analysis was performed for both the Russian GOST model [16] and the American NRLMSISE- 00 model [93]. Trajectory information for the calibration objects was taken from publicly available TLE data, although the efficient density-derivation algorithm by Picone et al. [77], discussed in Chap. 4, was not yet available to the researchers. Instead, the TLEs were processed into trajectories, which were used to estimate ballistic coefficients, containing information on the density model error.

A statistical analysis, investigating the possibility to predict correction parameters into the future has also been performed by this group [92]. As expected, the accuracy behaviour of predictions depends on the forecasting interval. While near-term results are significantly improved, forecasts over more than a few days can apparently no longer provide additional density accuracy over uncalibrated models.

2.5.3 The US Air Force Space Command HASDM Project

Another project, the United States Air Force Space Command's Dynamic Calibration Atmosphere (DCA) for the High-Accuracy Satellite Drag Model (HASDM) [87], used the tracking data from the Space Surveillance Network (SSN) directly, to adjust simultaneously the trajectories of around 75–80 calibration objects with spherical harmonic expansions of two temperature parameters from the Jacchia-70 thermosphere model [15]. Within Jacchia's models, these two temperatures define the vertical density profile completely. The spherical harmonic expansion allows corrections to the modelling of the diurnal variation. HASDM also includes a method for predicting the corrections three days into the future as a function of solar and geomagnetic indices.

A follow-on project, named Sapphire Dragon, was aimed at improving the prediction capabilities of HASDM through a series of enhancements, including an increase in the number of calibration objects and a more sophisticated use of various space weather proxies (*Bowman*, personal communication, 2006).

Unfortunately, the DCA calibrated model and the underlying precise SSN tracking data are not made publicly available. However, the HASDM model densities, computed along the CHAMP and GRACE tracks by Bruce Bowman, were kindly made available for evaluation. It is noteworthy that the density data derived from the SSN observations by Bowman et al. [8] have been used independently of HASDM as well. For instance, the data have been applied to study various modes of thermospheric forcing by Qian et al. [79–81].

2.5.4 ESA Funded Projects

Inspired by the first publications on the HASDM project, ESA's European Space Operations Centre ESOC funded a feasibility study [18, 26, 25] and software implementation [19, 20, 22] of thermosphere density model calibration using publicly available data. Although a number of different options were examined during the feasibility study, ultimately the choice was made to use TLE data, because of the near real-time data availability and the good spatial coverage if many objects are analysed simultaneously. The parameterisation schemes used by the US-Russian and HASDM projects were both implemented, adapted, and tested.

After the two ESOC projects were finalised, evaluation and improvement of the software have continued. First, the calibrated model was applied in the precise orbit determination of Earth observation satellites [21]. Later, the software was modified to use accelerometer-derived data from CHAMP and GRACE instead of TLE-derived data [23, 24].

Chapter 6 will cover the methods and a selection of the results from these investigations.

2.6 Tools for Evaluating Models and Observations

Further on in this thesis, the accuracy, resolution and other characteristics of thermosphere models and data sets will be evaluated. Several plotting and analysis methods that will aid in this endeavour are listed in the Sections below.

2.6.1 Plotting and Comparing Wide Ranges of Density Values

Density in the thermosphere ranges over many orders of magnitude, as a function of space and time (see Fig. 2.1). Sampling by different satellites in various orbits often results in a similarly wide-ranging data set. At first, this complicates the tasks of creating meaningful statistical comparisons and creating clear figures that retain visibility of interesting detail.

A straightforward and often applied solution is to use the logarithm of the densities to compress the range of values.

Another approach is to first convert the densities to equivalent exospheric temperatures, for example by inverting the CIRA- 72 algorithm for hydrostatic equilibrium. In this model, the exospheric temperature for a given epoch is modulated only by a fixed diurnal variation function. Therefore, temperatures derived for the same time, but at different locations from density observations of different satellites, can be compared with each other, and evaluated for consistency with this model. This straightforward link between temperature and density will form the basis of one of the density model calibration schemes, presented in Sect. 6.1.1. In a disturbed atmosphere, however, this equilibrium-based link between temperature and density can be too much of a simplification to allow for proper interpretation of the satellite data.

A third strategy to compress the range of values for further analysis is to normalise the density observations ρ_O by dividing them by equivalent model density values ρ_M, for the same time and location.

$$r = \frac{\rho_O}{\rho_M} \tag{2.14}$$

The resulting *density ratio* will generally fall in the range of about 0.5–2.0, depending on the combined error in the data and reference model. This much smaller range is suitable for incorporation in plots showing data from multiple satellites simultaneously, as will be done in Chap. 5. The ratios can also be used to either evaluate different density models using the same data set, or to identify outliers or erratic behaviour in contemporaneous data sets using the same model.

2.6.2 Density Evaluation Metrics

When evaluating density models, the deviation of the model with respect to an observation can be expressed as a percentage of the observation.

$$\epsilon = \frac{\rho_M - \rho_O}{\rho_O} \times 100\% \tag{2.15}$$

The Root-Mean-Square (RMS) of a set of these relative density error values will be used as a metric of density model accuracy. A possible disadvantage is that simple biases in the models or observations can not be distinguished from time-variable errors in this metric. It is therefore best suited when the mean with respect to the model has already been removed from the data. If this is not the case, a better approach is to use a two part metric, representing a mean and standard deviation. This leads us to the statistical distribution of density ratios.

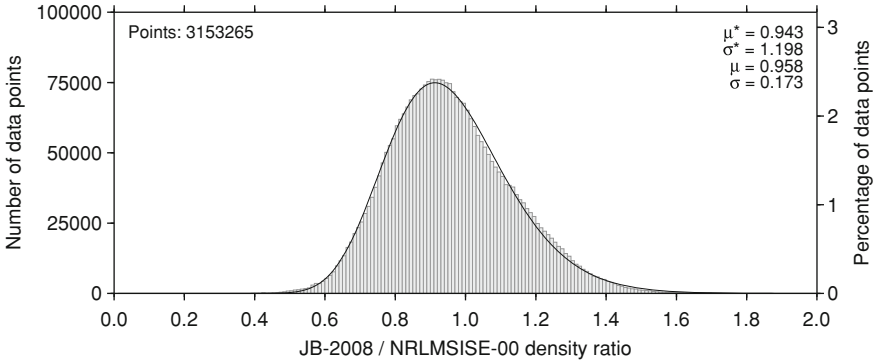

Fig. 2.11 Histogram showing the distribution of density ratios of two different models, evaluated along the CHAMP orbit during the year 2003. The log-normal distribution function, corresponding to the multiplicative mean μ^* and standard deviation σ^* of the data, is plotted with a *solid line*

2.6.3 Log-Normal Distribution of Density Ratios

Bezdèk [5] observed that the statistical relationship of the ratio of CACTUS accelerometer-derived densities and MSIS empirical model densities is consistent with the *log-normal distribution* [60]. This implies that the logarithm of the density ratios is approximately normal (Gaussian).

Figure 2.11 shows a histogram of density ratios for two empirical models. The data distribution is compared with an analytical log-normal distribution curve. Instead of the symmetrical bell-curve valid for Gaussian distributions, the log-normal distribution of the density ratios is skewed, with a shallower slope above the maximum and a steeper one below it. This is a consequence of the fact that the log-normal distribution is based on multiplication of random errors, while the Gaussian distribution is based on addition.

The Gaussian distribution is often used to characterise data sets with expressions such as $\mu \pm \sigma$, where the arithmetic mean μ and standard deviation σ are defining parameters of the distribution. These parameters can be used to express confidence intervals. There is an analogy for the log-normal distribution. Just as approximately 68.3% of the data lie within the mean, *plus or minus* one standard deviation, under a Gaussian bell-curve for normally distributed data, the same percentage of data lies within the log-normal mean μ^* *multiplied or divided by* the multiplicative standard deviation σ^* for log-normally distributed data. The minimum value of $\sigma^* = 1$ would indicate that the two density data sets are identical.

As we shall see in subsequent chapters, many (but not all) of the important error sources in deriving density data from satellite dynamics observations, such as the satellite frontal area and drag coefficient, are multiplicative in nature (see Sect. 3.2.1). Such errors scale the data, and thereby modify the log-normal mean. If the error is constant, the log-normal standard deviation will remain unaffected.

A comparison of density ratios using the Gaussian standard deviation can result in a misinterpretation of the results, because a scaling of the data set results in a modification of both the Gaussian mean and standard deviation.

2.6.4 Time Series, Binning and Gridding of Density Data

Further standard tools for analysing density models and observations, which will be used in subsequent chapters, include the display of time series, binning of data with respect to certain variables, computing statistics per bin and plotting the results in grids.

There are many variables which are interesting to use in plotting and/or binning density data or density ratios. We will discuss several important ones below. The reader is referred to Montenbruck and Gill [70] for additional details on orbital elements, time systems and coordinate systems.

In this thesis, time is expressed either with respect to the UTC or GPS systems. While UTC might be the preferred system for presentation of observation data, the CHAMP and GRACE data products are provided in GPS time. The difference between the two time systems, equal to the number of leap seconds introduced since January 1980, will be negligible in the plots.

Geodetic and geographic coordinates, including satellite altitudes, are computed with respect to the GRS 80 reference ellipsoid [71]. Geomagnetic coordinates are computed with respect to the IGRF dipole, based on the GEOPACK subroutine library by Dr. N. A. Tsyganenko.

As explained in Sect. 2.1.3, the local solar time is a measure of the longitudinal position of the satellite with respect to the sub-solar point. The related geocentric angle between the measurement location and the Sun can be useful in the analysis of density obtained near the perigee of elliptical orbits. It can be used to identify the position of the measurement with respect to the diurnal density bulge.

The *argument of latitude* ν is defined as the angle along the orbit from the ascending equator crossing. It is calculated by computing the Kepler elements of the osculating orbit, and summing the argument of perigee ω and true anomaly θ.

$$\nu = \omega + \theta \tag{2.16}$$

This variable is useful for plotting data from the CHAMP and GRACE accelerometer satellites, along their orbits. Values of $\nu = 0°$ and $\nu = 180°$ correspond to ascending and descending crossings of the equator. And since these missions have near polar orbit inclinations, values around $\nu = 90°$ and $\nu = 270°$ correspond to crossings of the North- and South-polar regions, respectively.

Finally, several analyses will show the relation of measurements with solar and geomagnetic activity levels, as represented by their proxies and indices described earlier in this chapter.

Examples of the analysis methods and plotting variables described above will be presented from Chap. 4 onwards. In the next chapter we will first focus on the

motion of the satellite in its orbit, and how it is affected by several forces, including the aerodynamic force.

References

1. Asikainen T, Maliniemi V, Mursula K (2010) Modeling the contribution of ring, tail and magnetopause currents to the corrected Dst index. J Geophys Res 115(A12203):16 doi:10.1029/2010JA015774
2. Barlier F, Berger C, Falin JL, Kockarts G, Thuillier G (1978) A thermospheric model based on satellite drag data. Ann Geophysique 34(1):9–24
3. Bartels J, Heck NH, Johnston HF (1939) Geomagnetic three-hour-range index measuring geomagnetic activity. J Geophys Res 44:411
4. Berger C, Biancale R, Ill M, Barlier F (1998) Improvement of the empirical thermospheric model DTM: DTM-94–a comparative review of various temporal variations and prospects in space geodesy applications. J Geod 72(3):161–178
5. Bezdèk A (2007) Lognormal distribution of the observed and modelled neutral thermospheric densities. Stud Geophys Geod 51(3):461–468 doi:10.1007/s11200-007-0027-2
6. Bowman BR, Tobiska WK (2006) Improvements in modelling thermospheric densities using new EUV and FUV solar indices. In: 16th AAS/AIAA space flight mechanics conference, Tampa Florida, pp 22–26, AAS 06-237, January 2006
7. Bowman BR (2004) The semiannual thermospheric density variation from 1970 to 2002 between 200–1100 km. In: AAS 04–174
8. Bowman BR, Marcos FA, Kendra MJ (2004) A method for computing accurate daily atmospheric density values from satellite drag data. In: 14th AAS/AIAA space flight mechanics conference, Maui Hawaii, February 8–12, 2004, AAS 04–173
9. Bowman BR, Tobiska WK, Marcos FA, Huang CY, Lin CS, Burke WJ (2008a) A new empirical thermospheric density model JB2008 using new solar and geomagnetic indices. In: AIAA/AAS Astrodynamics specialist conference and exhibit, pp 18–21 August 2008, Honolulu Hawaii, AIAA 2008–6438
10. Bowman BR, Tobiska WK, Marcos FA, Valladares C (2008) The JB2006 empirical thermospheric density model. J Atmos Sol Terr Phys 70(5):774–793 doi:10.1016/j.jastp.2007.10.002
11. Bruinsma S, Thuillier G, Barlier F (2003) The DTM-2000 empirical thermosphere model with new data assimilation and constraints at lower boundary accuracy and properties. J Atmos sol Terr Phys 65:1053–1070 doi:10.1016/S1364-6826(03)00137-8
12. Bruinsma S, Biancale R (2003) Total densities derived from accelerometer data. J Spacecraft Rockets 40(2):230–236
13. Cageao RP, Kerr RB (1984) Global distribution of helium in the upper atmosphere during solar minimum. Planet Space Sci 32(12):1523–1529 doi:10.1016/0032-0633(84)90019-9
14. Campbell WH (1996) Geomagnetic storms, the Dst ring-current myth and lognormal distributions. J Atmos Terr Phys 58(10):1171–1187 doi:10.1016/0021-916995001034
15. Casali SJ, Barker WN (2002) Dynamic calibration atmosphere (DCA) for the high accuracy satellite drag model (HASDM). In: AIAA/AAS astrodynamics specialist conference and exhibit, Monterey California, AIAA 2002–4888 5–8 August 2002
16. Cefola PJ, Nazarenko AI, Proulx RJ, Yurasov VS (2003) Atmospheric density correction using two line element sets as the observation data. In: AAS/AIAA astrodynamics specialists conference, Big Sky Montana, August 3–7, 2003, AAS 03–626
17. Domingo V, Fleck B, Poland AI (1995) The SOHO mission: an overview. Sol Phys 162 (1–2):1–37 doi:10.1007/BF00733425

18. Doornbos E (2004) Calibrated high accuracy satellite drag model - ESOC contract 16643/02/D/HK(SC) final report. Faculty of Aerospace Engineering Delft University of Technology, Delft The Netherlands
19. Doornbos E (2006) NRTDM final report - Near real-time density model (NRTDM) - ESOC contract 18576/04/D/HK(SC), Delft Institute for Earth-Oriented Space Research
20. Doornbos E (2007) Thermosphere density model calibration. In: Jean L (ed) Space weather, research towards applications in Europe, vol 344 of astrophysics and space science library, Springer
21. Doornbos E, Klinkrad H, Scharroo R, Visser P (2007) Thermosphere density model calibration in the orbit determination and prediction of ERS-2 and Envisat. In: Lacoste H (ed) Envisat symposium, Montreux, Switzerland, ESA SP-636, 23–27 April, 2007
22. Doornbos E, Klinkrad H, Visser P (2008) Use of two-line element data for thermosphere neutral density model calibration. Adv Space Res 41(7):1115–1122 doi:10.1016/j.asr.2006.12.025
23. Doornbos E, Förster M, Fritsche B, Van Helleputte T, Van den IJssel J, Koppenwallner G, Lühr H, Rees D, Visser P, Kern M (2009a) Air density models derived from multi-satellite drag observations. In: Proceedings of ESAs second swarm international science meeting, Potsdam Germany, 24–26 June 2009
24. Doornbos E, Förster M, Fritsche B, Van Helleputte T, Van den IJssel J, Koppenwallner G, Lühr H, Rees D, Visser P (2009b) ESTEC contract 21022/07/NL/HE Air density models derived from multi-satellite drag observations–final report, DEOS / TU Delft scientific report 01/2009, TU Delft
25. Doornbos EN, Klinkrad H (2006) Modelling of space weather effects on satellite drag. Adv Space Res 37:1229–1239 doi:10.1016/j.asr.2005.04.097
26. Doornbos EN, Klinkrad H, Visser PNAM (2005) Atmospheric density calibration using satellite drag observations. Adv Space Res 36:515–521 doi:10.1016/j.asr.2005.02.009
27. Drob DP, Emmert JT, Crowley G, Picone JM, Shepherd GG, Skinner W, Hays P, Niciejewski RJ, Larsen M, She CY, Meriwether JW, Hernandez G, Jarvis MJ, Sipler DP, Tepley CA, O'Brien MS, Bowman JR, Wu Q, Murayama Y, Kawamura S, Reid IM, Vincent RA (2008) An empirical model of the earth's horizontal wind fields: HWM07. J Geophys Res 113(A12304):18 doi:10.1029/2008JA013668
28. Dudok de wit T, Lilen sten J, Aboudarham J, Amblard P.O, Kretzchmar M (2005) Retrieving the solar EUV spectrum from a reduced set of spectral lines. Ann Geophys 23(9):3055–3069
29. Emmert JT, Picone JM (2010) Climatology of globally averaged thermospheric mass density. J Geophys Res 115(A09326):17 doi:10.1029/2010JA015298
30. Emmert JT, Drob DP, Shepherd GG, Hernandez G, Jarvis MJ, Meriwether JW, Niciejewski RJ, Sipler DP, Tepley CA (2008) DWM07 global empirical model of upper thermospheric storm-induced disturbance winds. J Geophys Res 113(A11319):113. doi:10.1029/2008JA013541
31. Escoubet CP, Schmidt R, Goldstein ML (1997) Cluster - science and mission overview. Space Sci Rev 79(1–2):11–32 doi:10.1023/A:1004923124586
32. Floyd L, Newmark J, Cook J, Herring L, McMullin D (2005) Solar EUV and UV spectral irradiances and solar indices. J Atmos Sol Terr Phys 3(15). doi:10.1016/j.jastp.2004.07.013
33. Forbes JM, Gonzalez R, Marcos FA, Revelle D, Parish H (1996) Magnetic storm response of lower thermosphere density. J Geophys Res 101(A2):2313–2319 doi:10.1029/95JA02721
34. Fuller-Rowell TJ (1998) The 'thermospheric spoon': a mechanism for the semiannual density variation. J Geophys Res 103(A3):3951–3956
35. Fuller-Rowell TJ, Codrescu MV, Moffett RJ, Quegan S (1994) Response of the thermosphere and ionosphere to geomagnetic storms. J Geophys Res 99(A3):3893–3914 doi:10.1029/93JA02015
36. Guo J, Wan W, Forbes JM, Sutton E, Nerem RS, Woods TN, Bruinsma S, Liu L (2007) Effects of solar variability on thermosphere density from CHAMP accelerometer data. J Geophys Res 112(A10308):13 doi:10.1029/2007JA012409

37. Hargreaves JK (1992) The solar-terrestrial environment: an introduction to geospace - the science of the terrestrial upper atmosphere ionosphere and magnetosphere vol 7 of cambridge atmospheric and space science series. Cambridge University Press, Cambridge
38. Harris I, Priester W (1962) Time-dependent structure of the upper atmosphere. J Atmos Sci 19(4):286–301
39. Heath DF, Schlesinger BM (1986) Mg 280-nm doublet as a monitor of changes in solar ultraviolet irradiance. J Geophys Res 91(D8):8672–8682
40. Hedin AE (1983) A revised thermospheric model based on mass spectrometer and incoherent scatter data - MSIS-83. J Geophys Res 88:10170–10188
41. Hedin AE (1988) The atmospheric model in the region 90 to 2000 km, Advances in Space Research, 8(5–6):(5)19–(5)25. In: COSPAR international reference atmosphere: 1986, Part I: Thermosphere models
42. Hedin AE (1991) Extension of the MSIS thermospheric model into the middle and lower atmosphere. J Geophys Res 96(A2):1159–1172
43. Hedin AE, Reber CA, Newton GP, Spencer NW, Salah JE, Evans JV, Kayser DC, Alcayde D, Bauer P, Cogger L (1977) A global thermospheric model based on mass spectrometer and incoherent scatter data MSIS. i - N2 density and temperature. J Geophys Res 82:2139–2147
44. Hedin AE, Reber CA, Newton GP, Spencer NW, Brinton HC, Mayr HG, Potter WE (1977) A global thermospheric model based on mass spectrometer and incoherent scatter data MSIS. II - composition. J Geophy Res 82:2148–2156
45. Hedin AE, Fleming EL, Manson AH, Schmidlin FJ, Avery SK, Clark RR, Franke SJ, Fraser GJ, Tsuda T, Vial F, Vincent RA (1996) Empirical wind model for the upper, middle and lower atmosphere. J Atmos Terr Phys 58(13):1421–1447 doi:10.1016/0021-916995001220
46. Hedin Alan E (1987) MSIS-86 thermospheric model. J Geophys Res 92(A5):4649–4662
47. Hedin Alan E et al (1988) Empirical global model of upper thermosphere winds based on atmosphere and dynamics explorer satellite data. J Geophys Res 93:9959–9978
48. Hedin Alan E et al (1991) Revised global model of thermosphere winds using satellite and groundbased observations. J Geophys Res 96(A5):7657–7688
49. Hickey MP (1988) The NASA Marshall engineering thermosphere model. NASA Marshall Space Flight Center, Alabama
50. Jacchia LG (1959) Two atmospheric effects in the orbital acceleration of artificial satellites. Nature 183(4660):526–527
51. Jacchia LG (1964) Static diffusion models of the upper atmosphere with empirical temperature profiles. Smithsonian astrophysical observatory special report 170
52. Jacchia LG (1971a) New static models of the thermosphere and exosphere with empirical temperature profiles. Smithsonian Astrophysical Observatory Special Report 313
53. Jacchia LG (1971b) Revised static models of the thermosphere and exosphere with empirical temperature profiles, Smithsonian Astrophysical Observatory Special Report 332
54. Jacchia LG (1972) Atmospheric models in the region from 110 to 2000 km. In: CIRA 1972: COSPAR International Reference Atmosphere. Akademie-Verlag, Berlin, pp 227–338
55. Jacchia LG (1977) Thermospheric temperature, density and composition: new models, Smithsonian Astrophysical Observatory Special Report 375
56. Kaiser ML (2005) The STEREO mission an overview. Adv Space Res 36(8):1438–1488 doi:10.1016/j.asr.2004.12.066
57. King-Hele D (1992) A tapestry of orbits. Cambridge University Press, Cambridge
58. Knipp DJ, Tobiska WK, Emery BA (2004) Direct and indirect thermospheric heating sources for solar cycles 21–23. Sol Phys 224(1–2):495–505 doi:10.1007/s11207-005-6393-4
59. Lean J (1991) Variations in the sun's radiative output. Rev Geophys 29(4):505–535 doi:10.1029/91RG01895
60. Limpert E, Stahel WA, Abbt M (2001) Log-normal distributions across the sciences: keys and clues. BioScience 51(5):341–352
61. Marcos FA (1990) Accuracy of atmospheric drag models at low satellite altitudes. Adv Space Res 10(3):417–422

62. Marcos FA, Kendra MJ, Griffin JM, Bass JN, Larson DR, Liu JJ (1998) Precision low earth orbit determination using atmospheric density callibration. J Astronaut Sci 46(4):395–409
63. Mayaud PN (1980) Derivation, meaning, and use of geomagnetic indices geophysical monograph 22. American Geophysical Union, Washington
64. Mayr HG, Harris I, Spencer NW (1978) Some properties of upper atmosphere dynamics. Rev Geophys Space Phys 16:539–565
65. McPherron RL, Baker DN (1993) Factors influencing the intensity of magnetospheric substorms. J Atmos Terr Phys 55(8):1091–1122 doi:10.1016/0021-9169(93)90040-6
66. Menvielle M, Berthelier A (1991) The K-derived planetary indices: description and availability. Rev Geophys 29(3):415–432
67. Menvielle M, Marchaudon A Geomagnetic indices in solar-terrestrial physics and space weather. In: Jean L (eds) Space weather research towards applications in Europe vol 344. Springer, Astrophysics and Space Science Library (2007)
68. Menvielle M, Paris J (2001) The aλ longitude sector geomagnetic indices. Contrib Geophys Geod 31(1):315–322
69. Moldwin M (2008) An introduction to space weather. Cambridge University Press, Cambridge
70. Montenbruk O, Gill E (2000) Satellite orbits - models, methods and applications. Springer-Verlag, Berlin
71. Moritz H (1980) Geodetic reference system 1980, Bulletin Geodesique
72. Owens JK (2002) NASA Marshall engineering thermosphere model - version 2 0 NASA/TM–2002–211786. Marshall Space Flight Center, Alabama
73. Paetzold HK, Zschorner H (1961) An annual and a semiannual variation of the upper air density. Pure Appl Geophys 48(1):85–92
74. de Pater I, Lissauer J (2001) Planetary sciences. Cambridge University Press, Cambridge
75. Paxton LJ, Christensen AB, Humm DC, Ogorzalek BS, Pardoe CT, Morrison D, Weiss MB, Crain W, Lew PH, Mabry DJ, Goldsten JO, Gary SA, Persons DF, Harold MJ, Alvarez B, Ercol CJ, Strickland DJ, Meng C-I (1999) Global ultraviolet imager (GUVI): measuring composition and energy inputs for the NASA thermosphere ionosphere mesosphere energetics and dynamics (TIMED) mission. Opt Spectrosc Tech Instrum Atmos Space Res III 3756(1): 265–276 doi:10.1117/12.366380
76. Picone JM, Hedin AE, Drob DP, Aikin AC (2002) NRLMSISE-00 empirical model of the atmosphere: statistical comparisons and scientific issues. J Geophys Res 107(A12):1468. doi:10.1029/2002JA009430
77. Picone JM, Emmert JT, Lean J (2005) Thermospheric densities derived from spacecraft orbits - I. Accurate processing of two-line element sets. J Geophys Res 110(A03301):19. doi:10.1029/2004JA010585
78. Prölss GW (2004) Physics of the Earth's Space Environment. Springer
79. Qian L, Solomon SC, Roble RG, Bowman BR, Marcos FA (2008) Thermospheric neutral density response to solar forcing. Adv Space Res 42(5):926–932 doi:10.1016/j.asr.2007.10.019
80. Qian L, Solomon SC, Kane TJ (2009) Seasonal variation of thermospheric density and composition. J Geophys Res 114(A01312). doi: 10.1029/2008JA013643
81. Qian L, Solomon SC, Mlynczak MG (2010) Model simulation of thermospheric response to recurrent geomagnetic forcing. J Geophys Res 115(A10301). doi: 10.1029/2010JA015309
82. Reber CA, Trevathan CE, McNeal RJ, Luther MR (1993) The upper atmospheric research satellite (UARS) mission. J Geophys Res 98(D6):10643–0647
83. Rees MH (1989) Physics and chemistry of the upper atmosphere cambridge atmospheric and space science series. Cambridge University Press, Cambridge
84. Roberts CE (1971) An analytical model for upper atmosphere densities based upon jacchia's 1970 models. Celestial Mech 4:368–377
85. Rottman G (2005) The SORCE mission. Sol Phys 230(1–2):7–25, doi:10.1007/s11207-005-8112-6
86. Sehnal L (1988) Thermospheric total density model TD. Bull Astron Institutes Czechoslovakia 39(2):120–127

87. Storz MF, Bowman BR, Branson JI, Casali SJ, Tobiska WK (2005) High accuracy satellite drag model (HASDM). Adv Space Res 36(12):2497–2505
88. Thuillier G, Bruinsma S (2001) The Mg II index for upper atmosphere modelling. Ann Geophys 19(2):219–228
89. Tobiska WK, Bouwer SD, Bowman BR (2006) The development of new solar indices for use in thermospheric density modeling. In: AIAA, AIAA 2006–6165
90. Troschichev O, Janzhura A, Stauning P (2006) Unified PCN and PCS indices: method of calculation, physical sense, and dependence on the IMF azimuthal and northward components. J Geophys Res 111(A05208):10. doi:10.1029/2005JA011402
91. Vallado DA (2001) Fundamentals of strodynamics and Applications. Second Edition: Microcosm Press, El Segundo, California
92. Yurasov VS, Nazarenko AI, Cefola PJ, Alfriend KT(2005a) Application of the ARIMA model to analyze and forecast the time series of density corrections for NRLMSIS-00. In: AAS/AIAA Astrodynamics specialist conference, Lake Tahoe, CA, August 7–11, 2005, AAS 05–256
93. Yurasov VS, Nazarenko AI, Cefola PJ, Alfriend KT (2005b) Density corrections for the NRLMSIS-00 atmosphere model. In: AAS/AIAA Space flight mechanics conference, Copper Mountain, Colorado, January 23–27, 2005, AAS 05–168
94. Zhang J, Richardson IG, Webb DF, Gopalswamy N, Huttunen E, Kasper JC, Nitta NV, Poomvises W, Thompson BJ, Wu C-C, Yashiro S, Zhukov AN (2007) Solar and interplanetary sources of major geomagnetic storms (Dst -100nT) during 1996–2005. J Geophys Res 112(A10102). doi:10.1029/2007JA012321